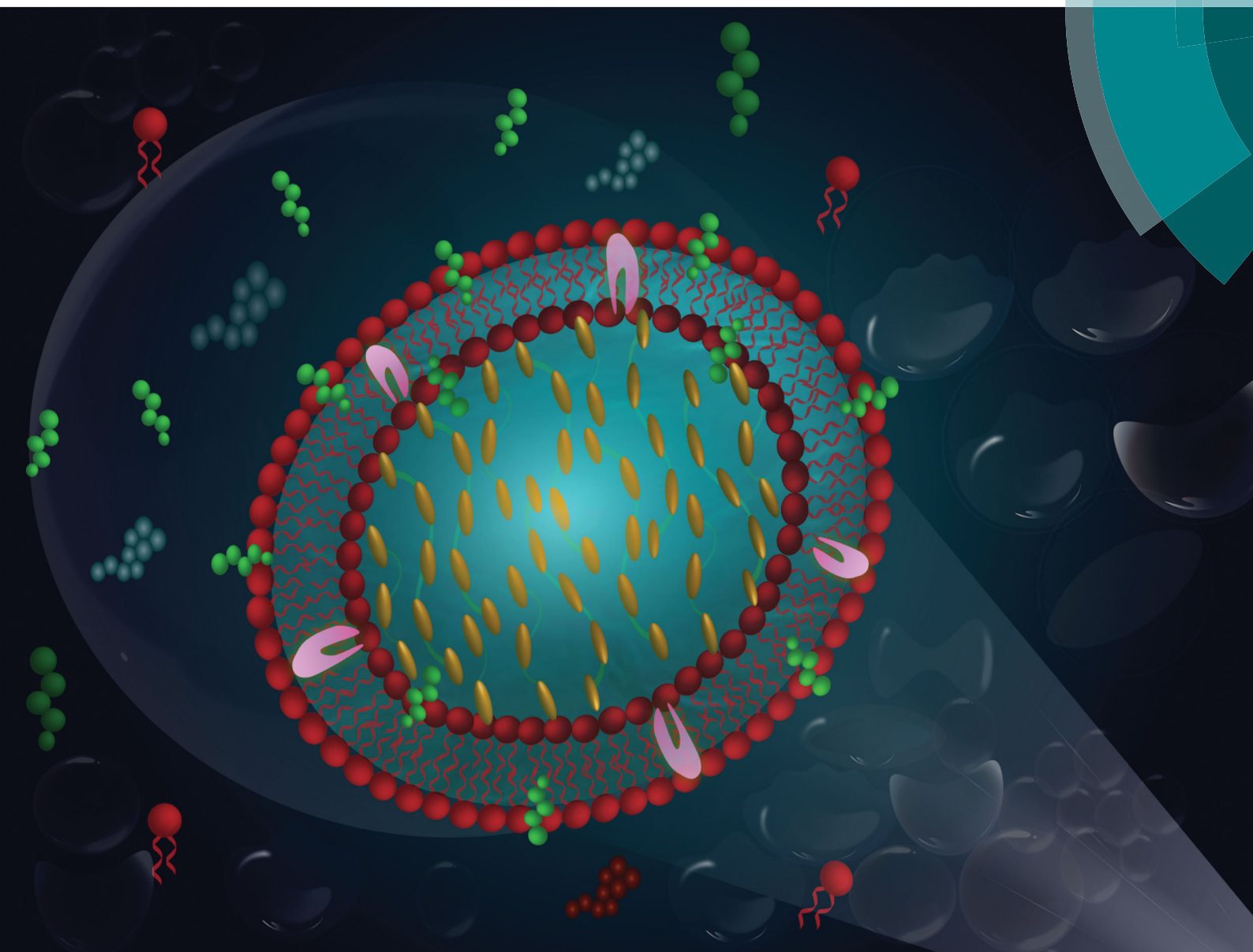


Soft Matter

rsc.li/soft-matter-journal



ISSN 1744-6848



PAPER

Alejandro D. Rey *et al.*
Morphology of elastic nematic liquid crystal membranes



Cite this: *Soft Matter*, 2017,
13, 5366

Morphology of elastic nematic liquid crystal membranes

Pardis Rofouie,^a Damiano Pasini^b and Alejandro D. Rey^{*a}

Liquid crystalline phases found in many biological materials, such as actin, DNA, cellulose, and collagen can be responsible for the deformation of cell membranes. In this paper, cell membrane deformation is investigated through the coupling between liquid crystal anisotropy and membrane bending elasticity. The generalized shape equation for anisotropic interfaces, which resort to the Cahn–Hoffman capillarity vector, the Rapini–Papoular anchoring energy, and the Helfrich elastic energy, is applied to gain insight into the deformation of closed liquid crystal membranes. This study presents a general morphological phase diagram of membrane surface patterns, in which two characteristic regimes of membrane shapes can be classified with respect to the most dominant factor between liquid crystal anisotropy and bending elasticity. To that end, we consider a 2D nematic liquid crystal droplet immersed in an isotropic phase in the presence of an interfacial layer of surfactants, which leads to an additional elastic contribution to the free energy of the system. The presented results indicate that, depending on the bending elasticity of the cell membrane, the liquid crystal might be able to deform the cell, thereby resulting in anisotropic asymmetric shapes. As liquid crystal anisotropy dominates the bending elasticity, spindle-like or tactoid shapes, which are extensively observed in experiments, can be formed. The findings provide a foundational framework to better understand membrane topologies in living soft matters. Furthermore, the coupling between order and curvature of membranes shed new light into the design of novel functional soft materials.

Received 16th May 2017,
Accepted 13th June 2017

DOI: 10.1039/c7sm00977a

rsc.li/soft-matter-journal

1. Introduction

Biological membranes show a wide variety of complex topographies and morphological instabilities. To elucidate the morphological variety of biological membranes, several theoretical studies were undertaken with the goal of minimizing membrane-bending energy subjected to area and volume constraints (Helfrich model, also known as the spontaneous curvature model).¹ Although Helfrich models can well capture numerous cell membrane morphological deformations, they fail to reproduce membrane shapes that are asymmetric, such as the echinocyte.² While the area difference elastic models (ADE), which minimize the energy associated with the area difference between the inner and outer leaflet of the membrane, can represent the top-bottom asymmetric.³ In these models, the membrane is considered as a 2D surface embedded in the 3D Euclidean space and assumed to exhibit purely elastic behaviour described by its mean curvature. Further, numerical simulations such coarse-grained molecular

dynamics (CGMD),⁴ spherical harmonics parameterization (SHP),⁵ and dissipative particle dynamics⁶ were proposed to provide a detailed description of pattern formation occurring in both symmetric and asymmetric deformation. Although significant progress has been made in formulating theoretical and numerical models that attempt to explore the complex surface morphologies in biological closed membranes, previous studies have been restricted to bilayer elastic models. There are few studies that consider other chemical and biological mechanisms (such as the presence of multiple components or in-plane orders) contributing to the formation of top-bottom asymmetric membrane shapes.⁷

As the lipid bilayers exhibit long range ordering,⁸ they might be regarded as liquid crystals. Furthermore, liquid crystalline phase and topological defects are found in numerous biological materials, such as DNA,⁹ cellulose,¹⁰ chitin,¹¹ collagen,¹² amyloid fibrils.¹³ Liquid crystallinity not only is governed most physical aspects of biological morphogenesis, but it also contributes in the detailed organization of cells and living tissues.¹⁴ A cell membrane can exhibit anisotropic behavior due to lipid tilt, lipid rotation, and chirality¹⁵ or due to external macromolecules like proteins.¹⁶ Liquid crystallinity of actin or tubulin polymer networks can also contribute in controlling shape deformation in biological cells.¹⁷ Besides, the morphological patterns of some

^a Department of Chemical Engineering, McGill University, 3610 University Street, Montreal, Quebec, H3A 2B2, Canada. E-mail: alejandro.rey@mcgill.ca;
Fax: +1 514 398-6678; Tel: +1 514 398-4196

^b Department of Mechanical Engineering, McGill University, 817 Sherbrook West, Montreal, Quebec, H3A 0C3, Canada

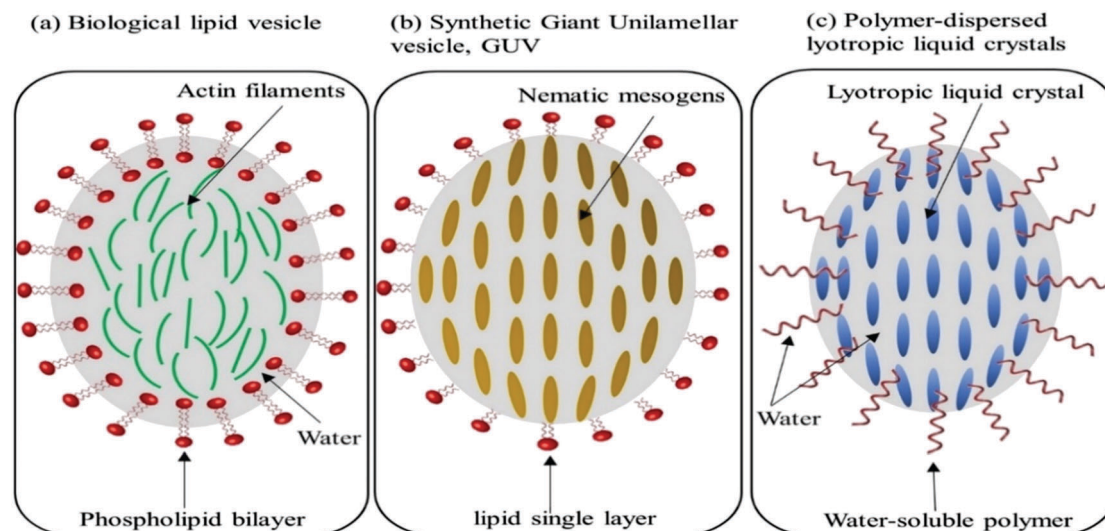


Fig. 1 Schematic of possible elastic anisotropic drops. (a) Liposome, (b) surfactant-coated nematic liquid crystal droplet, and (c) polymersome.

lyotropic liquid crystal droplets closely resemble the geometries and symmetries of living tissues and cell membranes.¹⁸ It is shown that spontaneous assembly of phospholipids at the interface between liquid crystals and aqueous phases results in dynamic spatial patterns typical of phospholipids.^{19,20} Another example of coupling between membrane elasticity and liquid crystal anisotropy responsible for the generation of complex surface morphologies, occurs in giant unilamellar vesicles (GUVs) suspended in a liquid crystal.²¹ Moreover, the three-dimensional architectures of some liquid crystal colloids closely resemble the geometries and symmetries of living tissues and cell membranes,^{7b} such as starfish morphology, an instance that confirms the analogy that can be drawn between liquid crystal anisotropy and amphiphilic surfactants.²² Polymersomes can also exhibit a large variety of morphologies that can be controlled by copolymer composition and subsequently respond to chemical or physical stimuli such as pH, osmotic pressure, and temperature.²³ This paper presents a systematic modeling approach to derive the equations coupling topology, elastic free energy, and anchoring conditions that can be used in analyzing the surface morphologies observed in elastic anisotropic drops such as liposomes or phospholipid bilayer, surfactant-coated nematic liquid crystal droplet or liquid-crystalline lipid monolayers, and polymersomes (see Fig. 1).

Several theoretical and experimental studies have been presented to model the coupling mechanism between the orientational order, topological defects, and the curvature in spherical vesicles.^{18,24} The presented theoretical studies illustrate the deformation of an isotropic droplet immersed in a liquid crystal phase^{24b} and the inverse problem, the deformation of a nematic liquid crystal droplet within an isotropic phase.^{24c} Recent studies have also explored the deformation of lyotropic chromonic liquid crystal (LCLC) drops²⁵ and active nematics.²⁶ For spherical nematic droplets, curvature generally drives formation of topological defects and disclinations, and correspondingly, defects and disclinations change curvature.^{21b} But, the nematic

droplets do not necessarily have a distorted director field. If the droplet size is sufficiently small, the director field would be homogenous and the droplet would be defect free, while large nematic droplets favor the formation of topological defects. The type of surface anchoring may result in the formation of either a hedgehog point defect in the center,²⁷ or a pair of surface point defects at the poles of the droplet known as boojums.²⁸ Other topological defects can be expected in 3D.²⁹ The results show that the equilibrium shape of nematic liquid crystal droplet is typically an ellipsoid in which the major axis of the shape lies along the director orientation.³⁰ The spindle-shaped droplet or tactoid have also been observed in suspensions where both isotropic and nematic phases exist.^{21a,24b,c}

Significant progress has been made in developing theoretical models that couple the orientational order and curvature for anisotropic elastic interfaces.³¹ We recently showed that when the liquid crystal anisotropy and bending effects are comparable, the planar anisotropic interface may show a rich variety of multi-scale complex patterns, such as spatial period-doubling, period-tripling, and quasi-periodicity.³¹ⁱ In this paper, we seek to characterize the shape deformation of closed liquid crystal membranes through the interaction of anisotropic interfacial tension, bending elasticity, and capillarity at free surfaces. We theoretically consider a nematic liquid crystal droplet immersed in a passive isotropic phase in the presence of an interfacial layer of surfactants, which leads to an additional elastic contribution to the free energy of the system. The aim of this work is to develop an exclusive physical model based on the integration of the Cahn–Hoffman capillarity vector developed for liquid crystals,^{31c} the classical Rapini–Papoular anchoring energy³² for liquid crystals, and the Helfrich membrane energy.³³ We only consider 2D drops, with a constant director field in its interior and with a surface that displays bending elasticity and anisotropic surface tension; the outer phase is inert.

As mentioned above we restrict the study to 2D cases, as in many previous works.^{1d,e} With this restriction the importance

of 3D effects, namely non-zero local Gaussian curvature are not captured. Local shapes in soft matter and hard matter are usually described in shape maps of Gaussian curvature in terms of average curvature,³⁴ where parabolic trajectories represent spheres and the zero Gaussian line represents a cylinder. With the 2D restrictions only shapes on the latter line are possible. In this study, since the Gaussian curvature is zero, the 3D extension of our 2D drop will be a cylindrical surface.³⁵ The radially symmetric cylinders, rods, are ubiquitous in walled cells such as bacteria, fungi, and plants.³⁶ Considering a 3D drop will be a challenging mathematical problem in which the proofs of existence, regularity of solutions, and measures of the non-uniqueness of solutions need to be established^{1d} in future work and is outside the scope of this paper.

Of particular interest here is to study the role of liquid crystal anisotropy in complex surface pattern formation. Understanding the mechanisms through which biological membranes exhibit specific morphologies can be used as an illustration of “bio-inspiration” for the design of novel devices such as sensors.

The specific objectives of this work are: (a) to derive and solve a nemato-capillary shape equation that describes the surface deformation of an elastic liquid crystal membrane; (b) to characterize the possible deformation modes and investigate the effect of the system physical parameters on the surface morphologies; (c) to characterize the role of membrane elasticity and anisotropic surface tension on the surface deformation mode; and (d) to elucidate the mechanisms that drive surface deformations.

The organization of this paper is as follows. Section 2 introduces the material model system, the different contributions to the free energy, and the governing nemato-capillary shape equation expressing the coupling mechanism between the surface geometry and director field in rectangular (x, y, z) coordinates. In this section, we assume a nematic liquid crystal membrane with quite weak homeotropic anchoring where the radius of the membrane is always significantly less than the extrapolation length scale, resulting in homogenous director field. Section 3 presents a phase diagram of liquid crystal membrane configurations as a function of the scaled pressure jump and the scaled LC anchoring, the effect of model parameters on the membrane shape. At the end of this section, a general morphological phase diagram of the surface patterns for the closed LC elastic membrane in the ternary parametric space (bending elasticity, anchoring, surface tension) is illustrated, which allows us to select the membrane shape that results from the interaction of the three primitive shapes (folded-shape, spindle-like, and ellipse). In Section 4, we present the capillary pressures associated with the bending-anchoring morphological instabilities. Section 5 presents the conclusions.

2. Theory and governing equations

In this section, we first present the material model system and the basic concepts of the membrane geometry. Then, we introduce

the governing nemato-capillary equations based on the widely used Cahn–Hoffman formalism³⁷ of capillarity for anisotropic closed membranes expressing the coupling mechanism between the surface geometry, membrane bending elasticity, and liquid crystal director field.

2.1. Geometry and structure

We note that in this paper we consider 2D drops and in 3D, these drops correspond to fibers whose axes are straight lines. The perimeter of the former correspond to the surface of the latter. For convenience we may refer to the membrane perimeter as the membrane surface, without any ambiguity.

The geometry of 2D nematic liquid crystal droplet immersed in an isotropic phase in the presence of an interfacial layer of surfactants or membrane can be characterized by a closed curve profile with respect to reference coordinates “ x – y ” (see Fig. 2). For circular membranes of radius of R , the curvature is constant through the perimeter. As the membrane deviates from that of a circle, the curvature varies around the circumference and is a function of the polar angle. In this work, the turning angle of the normal vector \mathbf{k} is used as a single scalar function $\varphi(s)$ to characterize the membrane profile in the x – y coordinates. s is the surface arc-length and L is the total system length. Knowing $\varphi(s)$, the membrane profile can be obtained by the integrals: $y = \int_0^L \cos \varphi ds$ and $x = \int_0^L \sin \varphi ds$.

The curvature is defined as the derivative of the normal angle: $\kappa = \frac{d\varphi}{ds}$. The area of the plane curve, A , can be computed as: $A = \int_0^L x \cos \varphi ds$. The unit tangent \mathbf{t} and the unit normal \mathbf{k} to the surface can be parametrized with the normal angle, $\mathbf{t}(\mathbf{x}) = (\sin \varphi(x), -\cos \varphi(x))$, $\mathbf{k}(x) = (\cos \varphi(x), \sin \varphi(x))$. The nematic liquid crystal orientation is defined by the director field

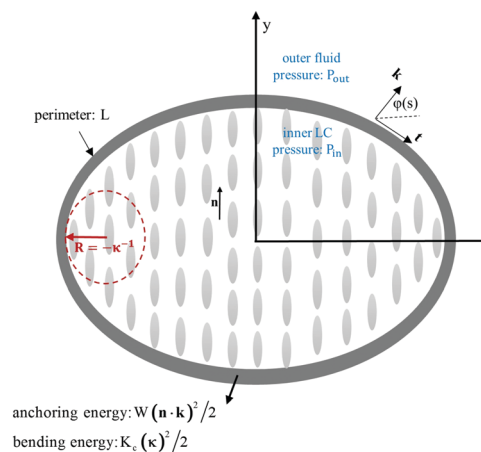


Fig. 2 Schematic of a 2D nematic liquid crystal drop covered by an elastic membrane immersed in an isotropic fluid. The rods denote the nematic director field. The director field is along the vertical “ y ” axis, the surface normal is \mathbf{k} , the surface tangent is \mathbf{t} , the normal angle is φ , and the total membrane length is L . W denotes the liquid crystal anchoring strength, k_c denotes the surface bending elasticity, and $\Delta p = p_{out} - p_{in}$ represents the pressure jump across the membrane. Note that the director field is constant everywhere and for this condition to exist the radius of the membrane is much less than the extrapolation length, K/W .

$\mathbf{n} \cdot \mathbf{n} = (\cos \theta, \sin \theta)$. The preferred orientation or easy axis at the interface can be parallel to the unit normal \mathbf{k} (homeotropic) or perpendicular to the unit normal \mathbf{k} (planar). It should be noted that the presence of surfactant-like biomolecules or phospholipids can change the preferred surface anchoring, and the director field.³⁸ For nematic liquid crystals immersed in aqueous surfactant solutions, it is shown that the anchoring type can depend on the surfactant's concentration, and increasing the surfactant concentration can lead to adsorption-driven orientational transition.³⁹ In this study, and without loss of physical phenomena, we restrict the discussion only to homeotropic anchoring ($W < 0$). To determine a closed surface profile for the membrane, a number of constraints must be imposed. Firstly, the membrane length L must satisfy the periodicity condition: $x(0) = x(L)$ and $y(0) = y(L)$. The smoothness of surface profile implies that $\kappa(0) = \kappa(L) = \kappa_0$. As the arc-length varies from 0 to L , the normal angle rotates from 0 to 2π indicating that there exists an integer m such that: $\oint \kappa ds = 2m\pi$.

2.2. Governing equations

The shape deformation of a liquid crystal (LC) membrane is a complex multiple-coupling problem that includes anisotropic surface tension, membrane bending elasticity, and Frank bulk elasticity.⁴⁰ To explore the shape selection of a liquid crystal membrane, the total system energy including the surface energy and the bulk Frank elastic energy should be minimized. However, the analytical solution of the problem with the usual formalism is very complicated. In this study, the bulk Frank elastic contribution to the shape equation is assumed to be negligible. The relative importance of the bulk elastic contributions compared to the anchoring energy can be evaluated by comparing the extrapolation length, $l_e = K/W$, (K being the Frank elastic constant) and the liquid crystal membrane radius, R . For a liquid crystal membrane with quite weak anchoring and small enough radius ($R \ll l_e$) the Frank elastic contribution is not significant as it scales as R , whereas the surface energy scale as R^2 . Consequently, the elastic energy dominates over the anchoring energy for small membranes, and we can assume that the director field is undistorted and homogenous.^{24b} The typical size of biological membranes is about $1 \mu\text{m}$.^{1a} Taking typical values of Frank elastic constant for nematic liquid crystals ($K \approx 10^{-12}$ – 10^{-11} N),⁴¹ the extrapolation length scale l_e is in the range of few micrometers ($l_e \simeq 10 \mu\text{m}$). Thus, to neglect the contribution of the elastic distortion, we should set the size constraint on the membrane ($R < 10 \mu\text{m}$). In this study, we are dealing with a quite weak anchoring, $W \simeq 10^{-6} \text{ J m}^{-2}$,⁴² and a relatively small value of the bending elasticity, $k_c \simeq 10^{-21}$ – 10^{-18} J ,⁴³ typical values for biological membranes, which gives a micron-range bending/anchoring length. We assume that the interfacial surface tension is $\gamma_0 = 10^{-7}$ – 10^{-5} N m^{-1} ,^{1a} and the pressure jump across the membrane is $\Delta p \simeq 0.1$ – 10 kPa .⁴⁴

Several theoretical models incorporating Helfrich membrane energy were formulated to investigate the shape deformation of

biological membranes and constrained soft materials.^{1c,d,43,45} In this section, we develop a physical model of a nematic liquid crystal membrane where the coupling mechanism between surface geometry and liquid crystal order is presented through the shape equation that resorts to the vector formalism of Cahn–Hoffman capillarity.³⁷ The presented liquid crystal Laplace–Helfrich shape equation can be employed to predict shape of isotropic droplet embedded in a nematic liquid crystal phase or shape of nematic liquid crystal embedded in an isotropic phase.

2.2.1. Cahn–Hoffman capillarity vector. The generalized Cahn–Hoffman capillarity vector ξ ³⁷ is the fundamental quantity that includes the curvature effects and liquid crystal orientation in one single vectorial quantity. The orientation-dependent surface energy can be specified by the unit vector or director $\mathbf{n} = \mathbf{n}(\mathbf{r})$ field, the surface position vector $\mathbf{r} = r\mathbf{k}$, and the surface unit normal \mathbf{k} . Cahn and Hoffman defined the nematic capillarity by the gradient of the scalar field $r\gamma$:

$$\xi(\mathbf{n}, \mathbf{k}) = \nabla[r\gamma(\mathbf{n}, \mathbf{k})] \quad (1)$$

For isotropic interfaces, the capillarity vector, ξ reduces to a normal vector $\xi = \gamma\mathbf{k}$. The decomposition of the surface director field into normal and tangential components yields $\mathbf{n}_\perp = \mathbf{k}\mathbf{k} \cdot \mathbf{n}$ and $\mathbf{n}_\parallel = \mathbf{I}_s \cdot \mathbf{n}$, where \mathbf{I}_s is the 2×2 unit surface dyadic $\mathbf{I}_s = \mathbf{I} - \mathbf{k}\mathbf{k}$, and \mathbf{I} is the 3×3 unit tensor. Calculating the gradient of the field $r\gamma$ appearing in eqn (1), using $\xi \cdot \mathbf{k} = \gamma(\mathbf{n}, \mathbf{k})$, $\xi \cdot d\mathbf{k} = d\gamma(\mathbf{n}, \mathbf{k})$, and $d(r\gamma) = \nabla(r\gamma) \cdot d\mathbf{r}$ gives:

$$\xi(\mathbf{n}, \mathbf{k}) = \gamma \frac{\partial r}{\partial \mathbf{r}} + r \frac{\partial \gamma}{\partial \mathbf{r}} = \underbrace{\gamma \mathbf{k}}_{\xi_\perp} + \underbrace{I_s \cdot \frac{\partial \gamma}{\partial \mathbf{k}}}_{\xi_\parallel} \quad (2)$$

where the normal component ξ_\perp describes the increase in the surface energy through dilation and the tangential component ξ_\parallel is the change in the surface energy through rotation of the unit normal. The surface energy that includes anchoring energy given by Rapini and Papoular³² and the Helfrich free energy³³ can be used to derive the Cahn–Hoffman capillarity vector ξ for a composite nematic liquid crystal membrane:

$$\gamma = \gamma_0 + \bar{k}_c K_G + 2k_c (H - H_0)^2 + \frac{1}{2} W (\mathbf{n} \cdot \mathbf{k})^2 \quad (3)$$

where γ_0 is the isotropic surface tension, k_c is the membrane bending elastic moduli, H is the membrane surface curvature, H_0 is the spontaneous curvature of the membrane, \bar{k}_c is the torsion elastic moduli of the membrane, and K_G is Gaussian curvature; based on the Gauss–Bonnet theorem⁴⁶ for closed membranes without edges the integral over the Gaussian curvature K_G is a topological invariant and it can be ignored.^{1e} The term $W(\mathbf{n} \cdot \mathbf{k})^2/2$ represents the anisotropic anchoring energy contribution due to the director field deviations from the preferred “easy axis”, and W is the surface anchoring strength. If $W > 0$, the easy axis or preferred orientation is tangential to the interface (planar), and if $W < 0$ the easy axis is normal to the interface (homeotropic anchoring). When the director field deviates from the preferred orientation, the deviation causes gradients in surface tension, and may generate the

orientational-driven tangential Marangoni elastic forces and as well as normal forces.⁴⁷ In this study, this Marangoni effect is neglected.

Substituting eqn (3) into eqn (2) yields the normal and tangential components of the capillarity vector:

$$\xi_{\perp}(\mathbf{n}, \mathbf{k}) = \left(\gamma_0 + \frac{W}{2}(\mathbf{n} \cdot \mathbf{k})^2 \right) - \frac{k_c}{2}\kappa^2 \quad (4a)$$

$$\xi_{\parallel}(\mathbf{n}, \mathbf{k}) = W((\mathbf{n} \cdot \mathbf{k})(\mathbf{n} \cdot \mathbf{t})) + k_c \frac{\partial \kappa}{\partial s} \quad (4b)$$

These equations show that when $\mathbf{n} \cdot \mathbf{k} = 1$, the surface behaves like an isotropic membrane and that the degree of anisotropy is controlled by $\mathbf{n} \cdot \mathbf{k}$.

2.2.2. Nematic-capillary shape equation. To derive the capillary shape equation required to determine the liquid crystal membrane shape, we use the capillary pressure definition $\Delta p = -\nabla_s \cdot \xi = -\nabla_s \cdot (\xi_{\perp} + \xi_{\parallel}) = -\mathbf{t} \cdot \frac{\partial \xi}{\partial s}$, where

$\frac{\partial \xi}{\partial s} = \frac{\partial \xi_{\parallel}}{\partial s} \mathbf{t} + \xi_{\parallel} \kappa \mathbf{k} + \frac{\partial \xi_{\perp}}{\partial s} \mathbf{k} - \xi_{\perp} \kappa \mathbf{t}$ yields:

$$\Delta p = -\mathbf{t} \cdot \frac{\partial \xi}{\partial s} = \xi_{\perp} \kappa - \frac{\partial \xi_{\parallel}}{\partial s} \quad (5)$$

By substituting the normal ξ_{\perp} and tangential ξ_{\parallel} components of the capillarity vector (eqn (4)) we obtain:

$$\Delta p = \left\{ \left(\gamma_0 + \frac{W}{2}(\mathbf{n} \cdot \mathbf{k})^2 \right) - \frac{k_c}{2}\kappa^2 \right\} \kappa - \left(k_c \frac{d^2 \kappa}{ds^2} + W(\mathbf{n} \cdot \mathbf{t})^2 \kappa \right) - W \left\{ (\mathbf{k} \cdot \mathbf{n}) \left(\mathbf{t} \cdot \frac{d\mathbf{n}}{ds} \right) + \mathbf{k} \mathbf{n} : \left(\frac{d\mathbf{n}}{ds} \right) \right\} \quad (6)$$

In the absence of the liquid crystal order, the contribution from the normal component of the capillary vector ξ_{\perp} is the classical Laplace pressure, and the contribution from the tangential component of the capillary vector ξ_{\parallel} , is known as Herring's pressure. For liquid crystal membranes, since the capillary vector is a function of both the director field, \mathbf{n} and the unit normal \mathbf{k} , an additional contribution to the capillary pressure arises from director curvature due to orientation gradients. This equation shows that the membrane shape is the result of the balance between the membrane bending elasticity, surface tension, surface anchoring effects, and the pressure jump. Both anchoring term and bending elasticity can drive shape deformation of a nematic liquid crystal membrane. Rearranging eqn (6), we obtain:

$$\frac{d^2 \kappa}{ds^2} = \frac{-1}{2}\kappa^3 + \frac{\gamma_0}{k_c}\kappa + \frac{-\Delta p}{k_c} + \frac{W}{2k_c}(\mathbf{n} \cdot \mathbf{k})^2 \kappa - \frac{W}{k_c}(\mathbf{n} \cdot \mathbf{t})^2 \kappa - \frac{W}{k_c} \left\{ (\mathbf{k} \cdot \mathbf{n}) \left(\mathbf{t} \cdot \frac{d\mathbf{n}}{ds} \right) + \mathbf{k} \mathbf{n} : \left(\frac{d\mathbf{n}}{ds} \right) \right\} \quad (7)$$

For nematic liquid crystal with the fixed director field, the director pressure term, $W\{(\mathbf{k} \cdot \mathbf{n})(\mathbf{t} \cdot d\mathbf{n}/ds) + \mathbf{k} \mathbf{n} : (d\mathbf{n}/ds)\}$

vanishes.⁴⁸ Integrating eqn (7) with respect to curvature κ , gives:

$$\frac{1}{2} \left(\frac{d\kappa}{ds} \right)^2 + \frac{1}{8}\kappa^4 - \frac{\gamma_0}{2k_c}\kappa^2 + \frac{\Delta p}{k_c}\kappa - \frac{W}{4k_c}(\mathbf{n} \cdot \mathbf{k})^2 \kappa^2 + \frac{W}{2k_c}(\mathbf{n} \cdot \mathbf{t})^2 \kappa^2 \quad (8)$$

In the absence of liquid crystal order, the integration can be reduced to:

$$\frac{1}{2} \left(\frac{d\kappa}{ds} \right)^2 + \frac{1}{8}\kappa^4 - \frac{\gamma_0}{2k_c}\kappa^2 + \frac{\Delta p}{k_c}\kappa \quad (9)$$

interpreting the quantity s as a time and κ as a position, eqn (9) corresponds to the equation of motion of a particle with unit mass and kinetic energy T , moving in a potential U and whose total energy E is conserved:

$$E = \frac{1}{2} \left(\frac{d\kappa}{ds} \right)^2 + \frac{1}{8}\kappa^4 - \frac{\gamma_0}{2k_c}\kappa^2 + \frac{\Delta p}{k_c}\kappa, \quad (10)$$

$$T(\kappa) = \frac{1}{2} \left(\frac{d\kappa}{ds} \right)^2, \quad U(\kappa) = \frac{1}{8}\kappa^4 - \frac{\gamma_0}{2k_c}\kappa^2 + \frac{\Delta p}{k_c}\kappa$$

The anchoring term in eqn (8) acts as the correction term when the mass of the particle changes with time.

Considering the nematic director field $\mathbf{n} = (\cos \theta, \sin \theta)$, surface unit normal $\mathbf{k}(s) = (\cos \varphi(s), \sin \varphi(s))$, unit tangent $\mathbf{t}(s) = (\sin \varphi(s), -\cos \varphi(s))$ and using the definitions: $\frac{dx}{ds} = \sin \varphi$, $\frac{d\mathbf{n}}{ds} = \frac{d\mathbf{n}}{dx} \frac{dx}{ds} = \frac{d\mathbf{n}}{dx} \sin \varphi$, $\kappa = \frac{d\varphi}{dx} \sin \varphi$ gives the governing shape equation:

$$\frac{d^3 \varphi}{ds^3} = -\frac{1}{2} \left(\frac{d\varphi}{ds} \right)^3 + \frac{-\Delta p}{k_c} + \frac{W}{2k_c}(\mathbf{n} \cdot \mathbf{k})^2 \left(\frac{d\varphi}{ds} \right) - \frac{W}{k_c}(\mathbf{n} \cdot \mathbf{t})^2 \left(\frac{d\varphi}{ds} \right) \quad (11)$$

The shape equation is a nonlinear third order ODE for the normal angle $\varphi(s, \Delta p, k_c, W, \gamma_0)$. In the absence of liquid crystal anisotropy, the eqn (11) becomes the classical Euler-Lagrange equation. It represents the interfacial force balance between the surface forces and the bulk force, $\Delta p \mathbf{k}$ due to the pressure jump across the membrane. The interfacial stress tensor \mathbf{T}_s can be expressed in terms of the capillary vector ξ :⁴⁹ $\mathbf{T}_s = \xi \cdot \mathbf{D}$ where $\mathbf{D} = \mathbf{k} \mathbf{I}_s - \mathbf{I}_s \mathbf{k}$ is the geometric tensor that maps the capillary vector into the tangential stress $\xi_{\perp} \mathbf{I}_s$ and bending stress $\xi_{\parallel} \mathbf{k}$. Then, the capillary pressure can be simply presented by: $\Delta p = (\nabla_s \cdot \mathbf{T}_s) \cdot \mathbf{k} = \nabla \cdot \xi$. The dot product of the interface stress tensor, \mathbf{T}_s with the unit tangent gives:

$$\mathbf{t} \cdot \mathbf{T}_s = \xi_{\perp} \mathbf{t} - \xi_{\parallel} \mathbf{k} \quad (12)$$

Besides, the normal vector, \mathbf{k} can be expressed as an arc-length derivative of a vector field: $\mathbf{k} = \frac{d}{ds}((\mathbf{r} \cdot \mathbf{t})\mathbf{k} - (\mathbf{r} \cdot \mathbf{k})\mathbf{t})$. Therefore, we can obtain:

$$\begin{aligned} \frac{\partial(\mathbf{t} \cdot \mathbf{T}_s)}{\partial s} &= \frac{\partial}{\partial s}(\xi_{\perp}\mathbf{t} - \xi_{\parallel}\mathbf{k}) = \Delta p \mathbf{k} \\ &= \Delta p \frac{d}{ds}((\mathbf{r} \cdot \mathbf{t})\mathbf{k} - (\mathbf{r} \cdot \mathbf{k})\mathbf{t}) \end{aligned} \quad (13)$$

Thus, the capillary shape equation can be readily found to be:

$$(\xi_{\perp}\mathbf{t} - \xi_{\parallel}\mathbf{k}) - \Delta p \mathbf{r} \cdot (\mathbf{t}\mathbf{k} - \mathbf{k}\mathbf{t}) = 0 \quad (14)$$

Multiplying the eqn (14) by $(\mathbf{k}\mathbf{t} - \mathbf{t}\mathbf{k})$ and considering that $(\mathbf{t}\mathbf{k} - \mathbf{k}\mathbf{t}) \cdot (\mathbf{k}\mathbf{t} - \mathbf{t}\mathbf{k}) = tt + kk$ results in:

$$(\xi_{\perp}\mathbf{k} + \xi_{\parallel}\mathbf{t}) = (-\Delta p)\mathbf{r} \quad (15)$$

Substituting the normal and tangential components of the capillary vector, eqn (4), we obtain:

$$\begin{aligned} \mathbf{r} &= \frac{\xi_{\perp}\mathbf{k} + \xi_{\parallel}\mathbf{t}}{(-\Delta p)}, \\ \mathbf{r} &= \frac{\left(\gamma_0 + \frac{W}{2}(\mathbf{n} \cdot \mathbf{k})^2 - \frac{k_c}{2}\kappa^2\right)\mathbf{k}}{(-\Delta p)} + \frac{\left(k_c \frac{\partial \kappa}{\partial s} + W((\mathbf{n} \cdot \mathbf{k})(\mathbf{n} \cdot \mathbf{t}))\right)\mathbf{t}}{(-\Delta p)} \end{aligned} \quad (16)$$

Thus, we can further find a notable polar formulation for computing the local radius of the nematic liquid crystal membrane:

$$\begin{aligned} r^2 &= \mathbf{r} \cdot \mathbf{r} = \frac{\xi_{\perp} \cdot \xi_{\parallel}}{(-\Delta p)^2}, \\ r^2 &= \frac{\left(\gamma_0 + \frac{W}{2}(\mathbf{n} \cdot \mathbf{k})^2 - \frac{k_c}{2}\kappa^2\right)^2}{(-\Delta p)^2} + \frac{\left(k_c \frac{\partial \kappa}{\partial s} + W((\mathbf{n} \cdot \mathbf{k})(\mathbf{n} \cdot \mathbf{t}))\right)^2}{(-\Delta p)^2} \end{aligned} \quad (17)$$

In the absence of liquid crystal anisotropy ($W = 0$), eqn (17) yields:^{1d}

$$r^2 = \frac{k_c E + \gamma_0^2}{\Delta p^2} + \frac{2k_c k}{\Delta p} \quad (18)$$

Using this equation, we can determine the local radius of the membrane for a known total energy E .

3. Results and discussion

To investigate the effects of the system physical parameters on the membrane shape and to characterize the morphological surface patterns, the nonlinear differential equation with periodic coefficients is solved using the AUTO software.⁵⁰ The reduced area of the membrane, the local curvature of the membrane, and the number of membrane folds are the important outputs of the model. The two significant parameters influencing the membrane morphology are: (i) the scaled anchoring coefficient, W/γ_0 (ii) the bending elasticity number, $\Delta p R_0^3/k_c$. The scaled anchoring coefficient W/γ_0 is taken to be in the range $0 < |W/\gamma_0| < 2$ (for nematic-air interface, the typical anchoring strength and surface tension is $W \approx 10^{-6} \text{ J m}^{-2}$ and $\gamma \approx 10^{-7}-10^{-5} \text{ J m}^{-2}$, respectively).⁴² The bending elasticity number, $\Delta p R_0^3/k_c$ is taken to be in the range $0.05 < \Delta p R_0^3/k_c < 50$ (typical value of bending elasticity and pressure jump across the membrane for biological membranes is $k_c \approx 10^{-21}-10^{-18} \text{ J}^{43}$ and $\Delta p \approx 0.1-10 \text{ kPa}$,⁴⁴ respectively).

Table 1 lists the system length scales, the dimensionless numbers, and their definitions and physical descriptions, that are captured in the results discussed below.

3.1. Shape selection

To find the shape of a nematic liquid crystal membrane, we first make eqn (11) dimensionless by taking $\tilde{s} = s/R_0$, $\alpha = \Delta p R_0^3/k_c$ (pressure bending number), $\beta = \gamma_0 R_0^2/k_c$ (tension bending number), $\omega = W R_0^2/k_c$ (anchoring bending number), where R_0 is the spontaneous radius of the membrane. We then have:

$$\begin{aligned} -\frac{d^3 \varphi}{d\tilde{s}^3} &= \frac{1}{2} \left(\frac{d\varphi}{d\tilde{s}} \right)^3 + \alpha - \beta \left(\frac{d\varphi}{d\tilde{s}} \right) - \frac{\omega}{2} (\cos^2(\varphi - \theta)) \left(\frac{d\varphi}{d\tilde{s}} \right) \\ &\quad + \omega (\sin^2(\varphi - \theta)) \left(\frac{d\varphi}{d\tilde{s}} \right) \end{aligned} \quad (19)$$

For each solution $\varphi = \varphi(\tilde{s})$ of eqn (19), there is a certain value of the variable \tilde{s} at which $d^2 \varphi / d\tilde{s}^2 = 0$. We choose $d^2 \varphi / d\tilde{s}^2 = 0$ at $\tilde{s} = 0$. We also select $d\varphi / d\tilde{s}|_{\tilde{s}=0} = d\varphi / d\tilde{s}|_{\tilde{s}=L/R_0}$ that gives closed solutions, and $\varphi|_{\tilde{s}=0} = \frac{\pi}{2}$, which is consistent with the homeotropic anchoring. Solving eqn (19) with the specified boundary conditions, we can investigate the shape selection of the membrane based on the three dimensionless parameters: α , β and ω . The spontaneous radius is fixed to ($R_0 = 0.5 \text{ }\mu\text{m}$) and

Table 1 System dimensionless numbers, their definitions and physical descriptions

Name	Symbol	Definition	Physical description
Bending elasticity number	α	$\Delta p R_0^3/k_c$	Ratio of the pressure jump and surface bending elasticity
Pressure bending number	β	$\gamma_0 R_0^2/k_c$	Ratio of the surface tension and surface bending elasticity
Anchoring bending number	ω	$W R_0^2/k_c$	Ratio of the anchoring and surface bending elasticity
Extrapolation length	l_e	K/W	Relative importance of the bulk elasticity to anchoring
Pressure bending length	ℓ_{pb}	$\sqrt[3]{\frac{k_c}{\Delta p}}$	Relative importance of the surface bending elasticity to pressure jump
Anchoring bending length	ℓ_{ab}	$\sqrt[2]{\frac{k_c}{W}}$	Relative importance of the surface bending elasticity to anchoring
Anchoring bending length	τ	L/ℓ_{ab}	Relative strength of the anchoring to the bending elasticity

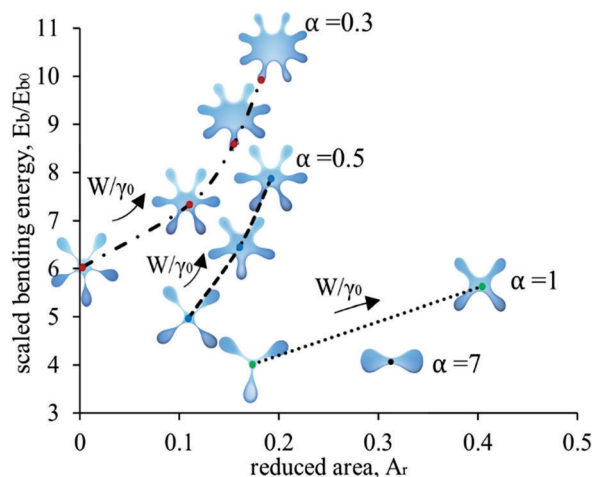


Fig. 3 The scaled bending energy as a function of the reduced area for four different values of the pressure bending dimensionless number $\alpha = 0.3, 0.5, 1$, and 7 . Increasing W/γ_0 results in deformation modes with increase the number of folds. The scaled bending energy increases with increasing number of folds. All the drops have a vertical mirror symmetry due to director axis orientation.

the remaining system parameters are varied to investigate their effect on the membrane shape selection.

To study the effect of the pressure bending number, α and the dimensionless anchoring number $W/\gamma_0 = \omega/\beta$ (ratio of the two other system dimensionless numbers ω/β) on the membrane shapes, the values for γ_0 , and R_0 are held fixed. The membrane shape can be characterized by the reduced area $A_r = 4\pi A/L^2$, where A is the membrane area and L is the membrane length and the dimensionless bending energy that is scaled by bending energy of the circular configuration, E_0 , with the reduced area ($A_r = 1$). Fig. 3 illustrates the dimensionless bending energy as a function of the reduced area for the n -fold membrane morphologies. For the morphologies shown in the beginning of each line (the left side of the lines), the corresponding scaled anchoring, W/γ_0 is zero. Thus, we can note that in the absence of liquid crystal anisotropy as the pressure bending number, α increases from 0.3 to 7 , the membrane shape is transformed from 5-fold (starfish) deformation mode to 2-fold deformation mode (discocyte), which is energetically less expensive than the starfish shape. These membrane shapes can be also obtained by minimizing the Helfrich free energy,^{1c,e} $\int_S \left(\gamma_0 + \frac{k_c}{2} \kappa^2 \right) ds + \int_S \Delta p dA$. All the shapes start as a circle for $A_r = 1$ and transform to the folded modes as A_r decreases from 1 .

In the presence of liquid crystal order with homeotropic anchoring, rising the dimensionless anchoring number, W/γ_0 , results in deformation modes with increased number of folds and higher bending energies. The results show that the anchoring energy can control the surface tension. This demonstrates an analogy between the liquid crystal anisotropy and the surface bending elasticity that can change the interfacial tension and drive the formation of several polymorphic topologies such as starfish membranes. In fact, the anchoring energy can govern

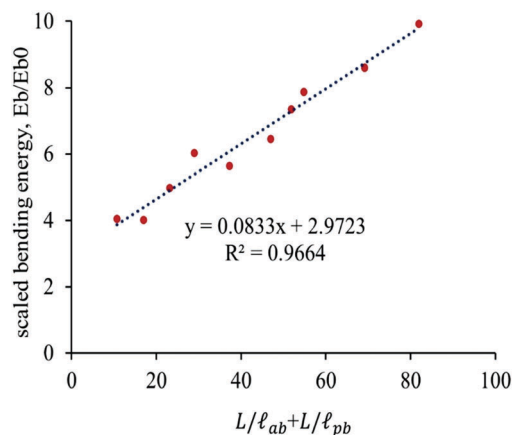


Fig. 4 Scaled bending energy as a function of total dimensionless length shows a linear scaling for the 2-fold, 3-fold, 4-fold, and 5-fold deformation modes.

the interfacial energy and lessen the energetic cost of creating multi-fold shapes. It should be noted that the shape deformation will only be significant for values of the scaled anchoring coefficient, $W/\gamma_0 \sim 1$ where the anchoring strength is of the same order, or larger, than the surface tension. For the morphologies shown in the beginning of the each line where the liquid crystal anisotropy is absent, increasing the surface tension, γ_0 above a threshold results in the self-intersecting membrane shapes.⁵¹ For instance, the discocyte shape intersects itself when the reduced area A_r becomes less than 0.3 .⁴⁵ As the self-intersecting shapes are physically irrelevant,^{1d} they are not discussed in the present work.

Fig. 4 shows the dimensionless bending energy of the membrane shapes corresponding to the 2-fold, 3-fold, 4-fold, and 5-fold modes, shown in Fig. 3 as a function of the total dimensionless length: $L/\ell_{ab} + L/\ell_{pb}$. The numerical results indicate that the bending energy of the folded membrane with constant surface tension is essentially a linear function of the scaled anchoring bending number, $\omega L/R_0$ and the scaled pressure bending number, $\alpha L/R_0$.

3.2. Effect of anchoring

In the presence of the nematic liquid crystal orientation, the surface area might be increased or decreased for the case of homeotropic or planar anchoring, respectively. Then, the excess or lack of the length might buckle the membrane shape. As an example, Fig. 5 shows the membrane shapes corresponding to the 2-fold, 3-fold, 4-fold, and 5-fold modes in the presence and absence of LC anisotropy. To investigate the effect of the liquid crystal anchoring W on the membrane shapes, for all the deformation modes the value of the surface tension, γ_0 is fixed. The break in top-to-bottom symmetry of the shapes occurred in the membranes with the presence of liquid crystal orientation is due to the competition between the bending elasticity of the membrane and the anchoring of the nematic liquid crystals.

It should be noted that adding the anchoring effect results in high curvature on the top of the membrane. The figure also illustrates that the 2-fold and 4-fold modes show the effect of

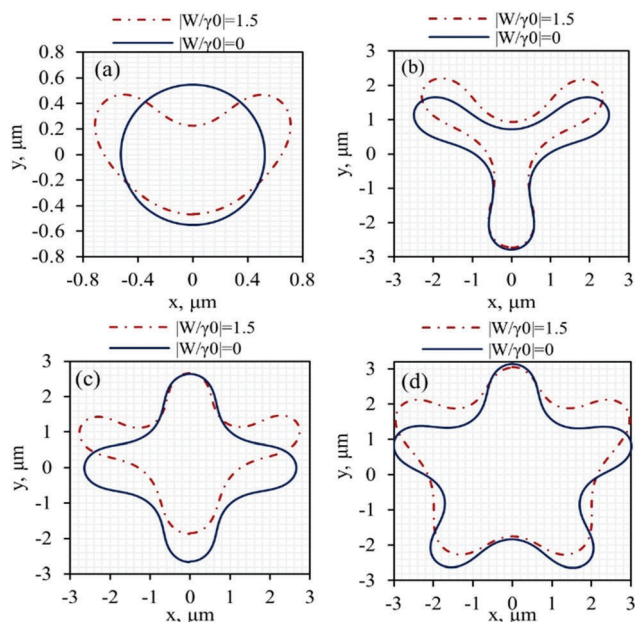


Fig. 5 Membrane shapes in the presence and absence of liquid crystal anisotropy. (a) 2-fold symmetry, (b) 3-fold symmetry, (c) 4-fold symmetry, and (d) 5-fold symmetry. The scaled anchoring coefficient is $W/\gamma_0 = 1.5$. The pressure bending number, $\alpha = \Delta p R_0^3/k_c$ and the tension bending number, $\beta = \gamma_0 R_0^2/k_c$ equal to $(\alpha = 2.5, \beta = 1.25)$, $(\alpha = 0.15, \beta = 0.075)$, $(\alpha = 0.08, \beta = 0.04)$, and $(\alpha = 0.05, \beta = 0.025)$ for Fig. 5(a) to (d), respectively. Adding the liquid crystal anchoring breaks the membrane top-to-bottom symmetry and results in high curvature on the top of the membrane shape.

greater top-to-bottom asymmetry with adding LC anisotropy. As the number of folds increases, the effect of anchoring in breaking the symmetry becomes insignificant. The reason is that the more folded modes corresponds to the higher bending energies where the anchoring energy has a slight effect on the membrane deformation shape. The 2-fold mode in the presence of the LC order shown in Fig. 5a is the known stomatocyte shape observed in red blood cell vesicles^{3b} that could not be obtained using the two-dimensional Helfrich model. So, by combining the two deformation mechanisms, bending and anchoring, in theory it would be possible to obtain the novel top-bottom asymmetric membrane shapes (Fig. 5(a–d), dashed lines), which are not possible configurations that can be produced using classical single-layer membrane models.

3.3. Effect of bending elasticity

To explore the effect of bending elasticity on the membrane shape, we varied the bending number, $\alpha = \Delta p R_0^3/k_c$ in a broad range from 0.05 to 50. It should be noted that the values for pressure jump Δp , and spontaneous radius R_0 are held fixed while k_c is varied. This range maps out a wide variety of membrane configurations. As shown in Fig. 6, a large part of the membrane shapes can be captured by varying a single parameter, the membrane bending elasticity, k_c . As the bending elasticity decreases, the number of membrane folds reduces and the morphology changes from 5-fold to discocyte, ellipsoid, stomatocyte, umbonate, umbilicate, and undulate. In the limit

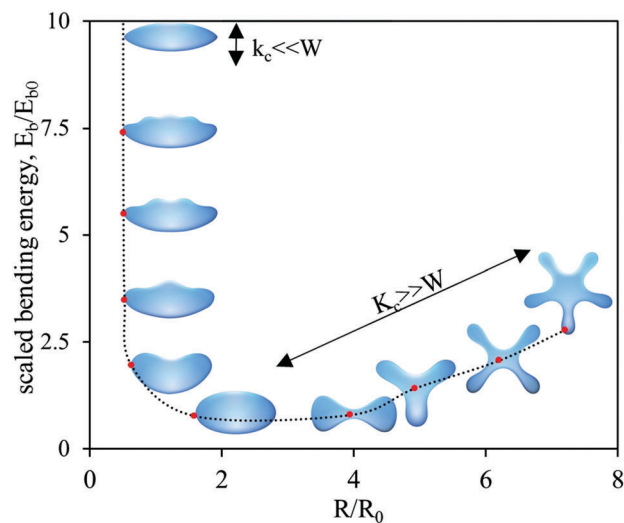


Fig. 6 Bending energy as a function of the ratio of radius of the membrane curvature to the spontaneous radius for a wide range of bending number $\alpha = 0.05$ –50. The values for pressure jump Δp , and spontaneous radius R_0 are held fixed while k_c is varied.

Table 2 Nomenclature of membrane morphologies

Shape	Name
	Discocyte
	Stomatocyte
	Umbonate
	Umbilicate
	Undulate
	Spindle-like shape

$k_c \rightarrow 0$ the shape of the membrane adapts to a spindle-like morphology. Table 2 lists the standard nomenclature of the membrane morphologies.

By decreasing k_c the ratio of radius of the membrane curvature to the spontaneous radius, R/R_0 which is also representative of the membrane reduced area, and the scaled bending energy decrease until the membrane shape adapts to the ellipsoid. Then, decreasing the bending elasticity further results in fixed reduced area (R/R_0) and increased scaled bending energy. Fig. 6 shows that two starkly different classes of membrane deformation modes can be characterized: n -fold topographies and 1-fold topographies, respectively, corresponding to the right nearly horizontal branch when the bending energy is dominant and the vertical left branch when both anchoring and bending contribute in buckling the membrane. The curvature of the liquid crystal membranes shown in the left branch can be very well approximated by Airy functions (see Appendix A). Earlier,

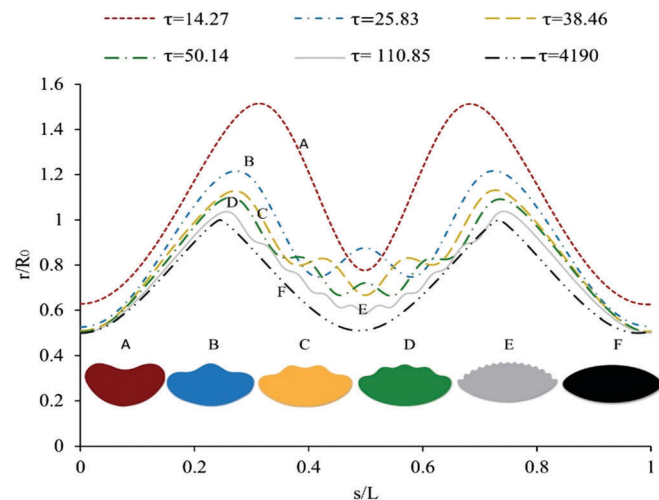


Fig. 7 The dimensionless local curvature, r/R_0 as a function of the scaled membrane arclength, s/L for six membrane morphologies with the different values of the dimensionless number τ . Through increasing τ , the dimensionless local curvature, r/R_0 shows period-doubling, period-tripling, period-quadrupling, and the high wavenumber periodic wrinkling of respectively corresponding to the discocyte, umbonate, umbilicate, and undulate morphologies (see Table 2).

boundary layer behavior of nematic liquid crystals in shear flows is analytically approximated in terms of Airy functions.⁵² The results show that when both liquid crystal anisotropy and membrane elasticity contribute in the membrane deformation, the anchoring strength promotes shape anisotropy and top-to-bottom asymmetry while the membrane elasticity promotes symmetric shapes. Thus, the complex morphologies (shown in the left vertical branch of Fig. 6) that emerge in numerous biological membranes can also be explored by another mechanism that couples liquid crystal orientational order and membrane elasticity and be well described by a fundamental function (Airy) of physics.

To explore the morphological patterns shown in the left vertical branch of Fig. 6, we present in Fig. 7 the dimensionless local curvature, r/R_0 (see eqn (17)) as a function of the scaled membrane arclength, s/L for six membrane morphologies with the different values of the dimensionless number τ . The dimensionless parameter, τ is a measure of the relative strength of the liquid crystal anchoring to the bending elasticity. As the liquid crystal anisotropy can compete with the bending elasticity, a range of multiple wavelengths pattern can form. Through increasing the effect of liquid crystal anisotropy, first, the period-doubling pattern corresponding to the discocyte shape appears. Then, period-tripling, period-quadrupling, and the high wavenumber periodic wrinkling respectively corresponding to the umbonate, umbilicate, undulate appear. As the bending elasticity becomes insignificant, the surface undulations disappear and the membrane shape adopts the spindle-like morphology.

An increase of the effect of liquid crystal anisotropy decreases the periodicity of the wrinkles and leads to the higher wavenumber periodic patterns. The greater the value of τ , the smaller

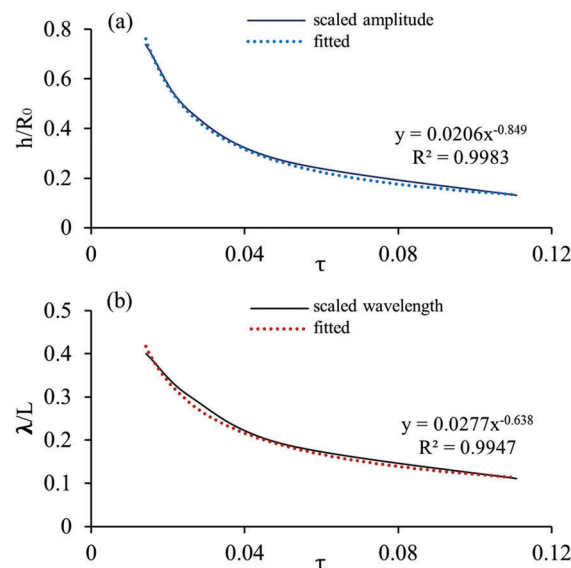


Fig. 8 Effect of the dimensionless number τ on (a) the scaled amplitude and (b) the scaled wavelength of the smooth wrinkles. The dotted lines illustrates the best power-law fits for the scaled amplitude and wavelength.

are the amplitudes and the wavelength of the smooth wrinkles, as shown in Fig. 8.

3.4. Membrane elongation

The membrane elongation can be characterized by its aspect ratio $\varepsilon = b/a$. The effect of the dimensionless number τ on the membrane elongation is shown in Fig. 9. In the absence of LC anisotropy, for quite small bending elasticity the membrane will tend to be close to an ellipsoid so as to minimize their interfacial energy. In the presence of liquid crystal anisotropy, when the anchoring coefficient is of the same order, or larger than the surface tension, the nematic liquid crystal membrane has spindle-like shape. The aspect ratio of the membrane we obtained obeys $\frac{b}{a} = 96.06\tau$ if $\tau \ll 0.05$ and $\frac{b}{a} = 1.27\tau$ if $\tau \gg 0.05$,

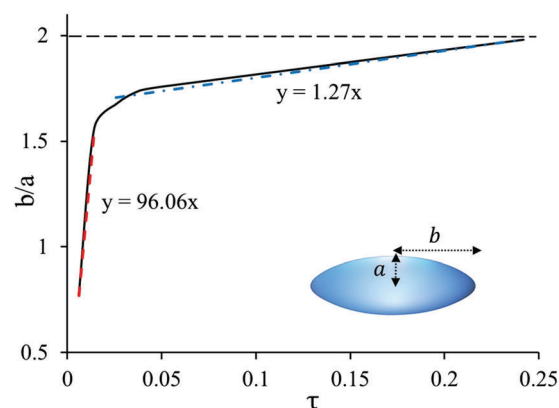


Fig. 9 Aspect ratio, b/a of a homogeneous nematic membrane as a function of the dimensionless number, τ . The aspect ratio of the membrane shows a linear relationship, $\frac{b}{a} = 96.06\tau$ if $\tau \ll 0.05$ and $\frac{b}{a} = 1.27\tau$ if $\tau \gg 0.05$. The dashed black line illustrates the points where the membrane shape has a constant aspect ratio, $b/a = 2$.

which is quite close to the approximate results presented by ref. 24c.

In the absence of bending elasticity, the aspect ratio of the nematic liquid crystal droplet predicted using the Wulff construction shows a linear relationship, $\frac{b}{a} = 1 + W/\gamma_0$ if $W/\gamma_0 \ll 1$ and a power function, $\frac{b}{a} = \left(\frac{W}{\gamma_0}\right)^{1/2}$ if $W/\gamma_0 > 1$. As we expect that by increasing the dimensionless number, τ , the aspect ratio of the membrane becomes a weak function of the dimensionless anchoring. In Fig. 9, the dashed black line illustrates the points where the membrane shape has a constant aspect ratio, in this case equals to $b/a = 2$. Regardless of whether the anchoring type is homeotropic or planar, the liquid crystal membrane favors elongated shapes.

The elongation follows the liquid crystal director field. Here, as homeotropic anchoring is preferred, any deviation from a spherical shape will result in an ellipsoid whose axis is perpendicular to the director field. However, in the case of planar anchoring (not treated here), the main axis of the membrane is parallel to the director field. Also, it should be noted that for small values of the scale anchoring coefficient, W/γ_0 where the isotropic surface tension γ_0 , dominates the anisotropic surface tension, the membrane tip becomes rounded. The increase in anisotropic surface energy compensates with the shorter total boundary length associated with rounded tips.⁵³ While for sufficiently large values of the scaled anchoring coefficient, W/γ_0 , the opposite condition occurs and the tip becomes sharp. As reported in ref. 24b, the aspect ratio of the nematic liquid crystal droplet decreases with decreasing the dimensionless parameter, $\beta = \gamma_0 R_0^2/k_c$ which is a measure of the relative strength of the surface tension to bending elasticity. For membrane with spindle-like shapes, the effect of the membrane elasticity would be to remove the sharp discontinuity in curvature, which minimize the curvature energy. In agreement with the earlier works,^{24c,54} the membrane would be spherical if $W/\gamma_0 \approx 0$, elongated if $0 < W/\gamma_0 \leq 1$, and elongated with sharper ends if $W/\gamma_0 > 1$.

3.5. Morphological phase diagram

To obtain a comprehensive atlas of morphological surface patterns, and to predict the membrane shapes depending on the system physical parameters, we present in Fig. 10 the general morphological phase diagram of the surface patterns for a liquid crystal membrane with a constant pressure jump across the membrane, $\Delta p = 1$ kPa, in a ternary parametric shape space (k_c , W , γ_0). The fundamental membrane shapes at the corners of the triangle are: spindle-like shape (top) with nearly zero bending elasticity (liquid crystal droplet), ellipse (lower right) with zero bending and zero anchoring, and n -fold pattern (lower left) with zero anchoring. In the triangle's interior, the liquid crystal anisotropy competes with the bending elasticity, and promotes formation of surface patterns with increased number of folds and higher bending energies. But, for the cases bending elasticity is higher than $k_c > 5 \times 10^{-21}$ J, the effect of liquid crystal anchoring is insignificant, and the membrane practically adopts

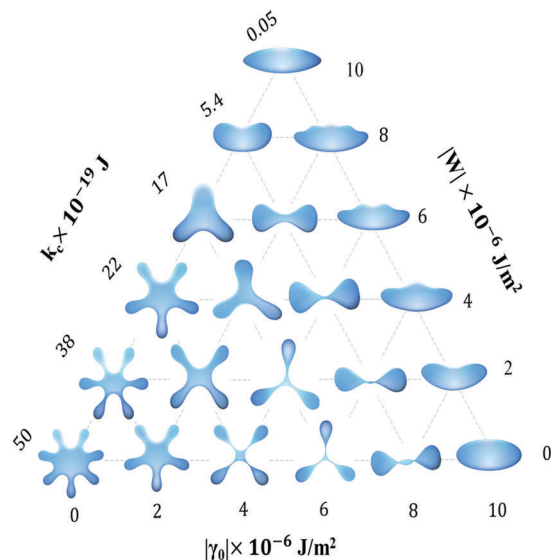


Fig. 10 The ternary phase diagram (k_c , W , γ_0) of the membrane surface morphologies. Surface pattern selection mostly depends on anchoring strength W and bending elasticity k_c . The n -fold pattern appears at high bending elasticity and weak anchoring, the spindle-like shape occurs at strong anchoring and low bending elasticity. The top-bottom asymmetric pattern is observed where both bending elasticity and anchoring strength are comparable.

the conventional bending elastic shapes. For the minimum value of the bending elasticity, $k_c = 5 \times 10^{-21}$ J (the right side of the triangle), the both liquid crystal anisotropy and membrane elasticity can equally contribute in the membrane deformation. The anchoring strength promotes the shape anisotropy and the top-to-bottom asymmetry, and creates the complex morphologies such as discocyte, ellipsoid, stomatocyte, umbonate, umbilicate, and undulate. With the increase of anchoring, the smooth surface undulations on the top of the membrane disappear and the membrane shape adopt the spindle-like morphology. Increasing the surface tension, γ_0 particularly when the anchoring strength is insignificant results in the self-intersecting membrane shapes. In general, we can identify two main surface patterns: symmetric and asymmetric. The first is located at the limiting cases of zero anchoring/high bending elasticity.

In the absence of anchoring (the base of the triangle), the surface patterns correspond to the classical folded elastic membrane shapes. With the decrease of bending elasticity, the surface patterns change into modes with lower number of folds, while for the minimum value of the bending elasticity $k_c = 5 \times 10^{-21}$ J, the membrane in the absence of anchoring forms the ellipse (shown in the lower right corner of the ternary phase diagram). As the value of bending elasticity is nearly zero (with $k_c = 0$, the shape equation approaches infinity), the membrane shape is not a circle but ellipse. In partial summary, if the effect of the bending elasticity is predominant, the membrane shape is a n -fold pattern. If the effect of anchoring is predominant, the membrane shape is a spindle-like. When both effects are comparable, the membrane exhibits top-bottom asymmetric patterns, as illustrated in the right side of the triangle.

We can conclude that the morphology phase diagram can allow us to determine what characteristic pattern will appear on the surface membrane based on the interaction of the three primitive shapes (n -fold, spindle-like shape, and ellipse). We can also gainfully compare the fundamental topographies of closed membrane with the three primitive surface wrinkling of planar liquid crystal membranes, where the n -fold, spindle-like, and ellipse shapes of the closed membrane are identical to folding, creasing, and flat patterns observed in the planar liquid crystal elastic membrane, respectively.³¹ⁱ

4. Pattern formation mechanism, pressure–curvature relations

To assign real forces behind shape selection we examine all the acting pressures across the surface. Rearranging eqn (19) gives the four scaled surface pressures as function of the scaled membrane arc-length, $\tilde{s} = s/R_0$:

$$\frac{\Delta p R_0^3}{k_c} = \underbrace{-\left(\frac{d^3\varphi}{d\tilde{s}^3} + \frac{1}{2}\left(\frac{d\varphi}{d\tilde{s}}\right)^3\right)}_{P_{\text{bending}}} + \underbrace{\frac{\gamma_0 R_0^2}{k_c} \left(\frac{d\varphi}{d\tilde{s}}\right)}_{P_{\text{dilation}}} + \underbrace{\frac{W R_0^2}{2k_c} (\cos^2(\varphi - \theta)) \left(\frac{d\varphi}{d\tilde{s}}\right) - \frac{W R_0^2}{k_c} (\sin^2(\varphi - \theta)) \left(\frac{d\varphi}{d\tilde{s}}\right)}_{P_{\text{rotation}}} + \underbrace{\frac{W R_0^2}{2k_c} (\cos^2(\varphi - \theta)) \left(\frac{d\varphi}{d\tilde{s}}\right)}_{P_{\text{jump}}} \quad (20)$$

The bending elastic pressure, P_{bending} captures the membrane's resistance to bend (increasing energy with increasing area), while the Herring's capillary pressure, P_{rotation} is the driving force

that undulates the membrane interface. The surface wrinkling emerge in response to competition between the bending resistance, which favors the large wavelengths, and the rotation pressure that favors the smooth wrinkles. To identify the mechanisms behind LC-elastic wrinkling, the four system scaled pressures: P_{bending} , P_{dilation} , P_{rotation} , and P_{jump} are illustrated as function of the scaled membrane arc-length, s/L for four membrane morphologies with different dimensionless numbers, $\left(\sqrt{\frac{2WL^2}{k_c}}\right)$ (see Fig. 11). The figure demonstrates that

for the stomatocyte, umbilicate, and undulate morphologies, the scaled bending pressure and the scaled dilation pressure are quite out-of-phase while the rotation pressure changes its phase along the membrane arc-length, such that in some parts P_{rotation} and P_{bending} are in-phase while P_{rotation} and P_{dilation} are out-of-phase, and in some parts, P_{rotation} and P_{dilation} are in-phase while P_{rotation} and P_{bending} are out-of-phase. The stress jump pressure is always negative, and as the dimensionless number τ increases, its contribution to the surface wrinkling becomes insignificant. The key observation from these pressure profiles is that in the middle of the membrane arc-length ($s/L = 0.5$) dilation and rotation pressures are always in-phase, and bending pressure are always out-of-phase with the dilation and rotation pressures. For the spindle-like shape morphology (Fig. 11d), where the bending pressure is close to zero, the dilation pressure and rotation pressure is always out-of-phase. Fig. 11 also illustrates that all surface capillary pressures grow as the dimensionless number τ increases, while the stress jump remains constant. Increasing the dimensionless number τ changes the degree of asymmetry between the top and bottom of the membrane (where the strong surface anchoring, top-bottom asymmetric

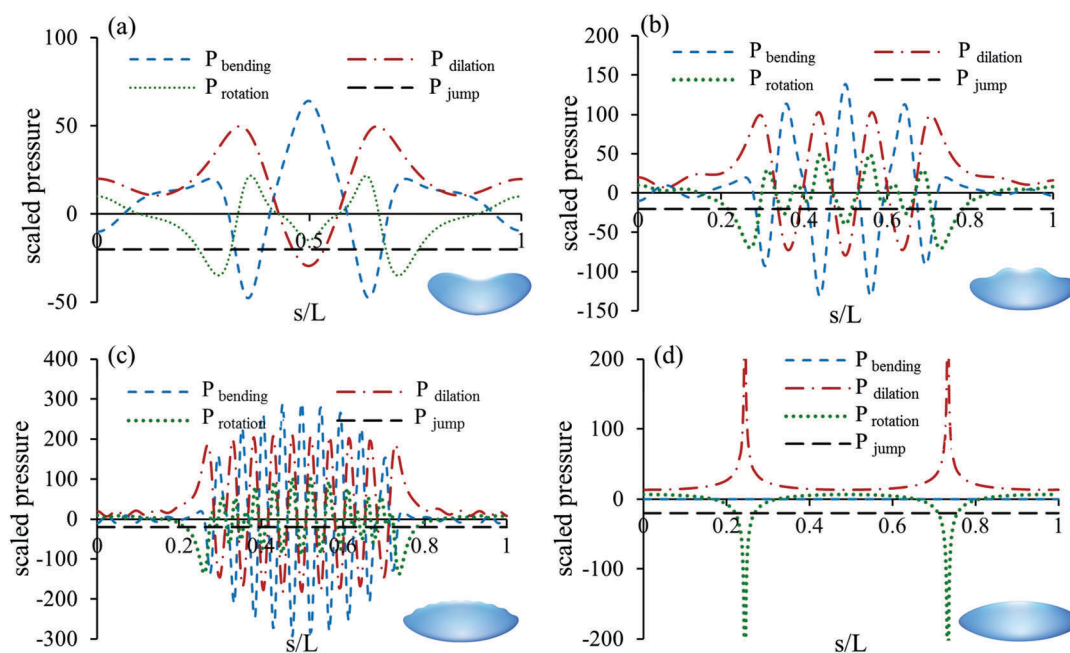


Fig. 11 The scaled pressures: P_{bending} , P_{dilation} , P_{rotation} , and P_{jump} are illustrated as function of the scaled membrane arc-length, s/L for four membrane morphologies with the different dimensionless numbers, (a) $\tau = 14.27$, (b) $\tau = 38.46$, (c) $\tau = 110.85$, and (d) $\tau = 500$.

membrane shapes emerge, and the surface energy increases by increasing the surface area) while for the spindle-like morphology, the wrinkles disappear and the membrane becomes symmetric.

5. Conclusions

In this paper, we have presented a physical model based on the elasto-capillary shape equations to study the surface pattern formation in closed liquid crystal elastic membranes. Using the presented model, we can obtain well-defined families of membrane morphologies. Besides, we showed that the complex morphologies that emerge in numerous biological membranes can be systematically explored by the mechanism that couples liquid crystal orientational order and membrane elasticity. The results show that when both liquid crystal anisotropy and membrane elasticity contribute in the membrane deformation, the anchoring strength promotes shape anisotropy and top-to-bottom asymmetry while membrane elasticity promotes symmetric shapes. We presented a general morphological phase diagram of the membrane surface patterns, in which we classify two characteristic regimes of membrane shapes based on whether the liquid crystal anisotropy or bending elasticity is dominant. The phase diagrams allow us to determine what membrane shape will form based on the interaction of the three primitive shapes (ellipse, spindle-like shape, and n -fold). A one-to-one mapping of this primitive drop shapes with wrinkling-creasing-flat shape of open surfaces was established. The complex pressure balances behind shape selection was demonstrated. The observation of complex top-bottom asymmetric topographies in biological membranes can now be understood in terms of liquid crystal anisotropy and we can conclude that numerous surface morphologies observed in living cells might be formed through coupling between liquid crystal anisotropy and bending elasticity. All these findings provide a foundation to understand the pattern formation in biological cell membranes and open up new opportunities to design novel anisotropic soft materials with unique optical and wetting functionalities such as biosensors and superhydrophobic grating surfaces.

Appendix A: Airy function

The Airy functions of the first and second kind, Ai and Bi which commonly appear in physics, especially in optics, quantum mechanics are the independent solutions to the homogenous second order differential equation, $y'' - xy = 0$:⁵⁵

$$\text{Ai}(x) = \frac{1}{\pi} \int_0^\infty \cos\left(\frac{z^3}{3} + xz\right) dz \quad (\text{A1})$$

$$\text{Bi}(x) = \frac{1}{\pi} \int_0^\infty \left[e^{-z^3/3+xz} \sin\left(\frac{z^3}{3} + xz\right) \right] dz \quad (\text{A2})$$

The Airy function Gi is the independent solution to the inhomogeneous second order differential equation, $y'' - xy = \pm\pi^{-1}$:⁵⁵

$$\text{Gi}(x) = \frac{1}{\pi} \int_0^\infty \sin\left(\frac{t^3}{3} + xt\right) dt \quad (\text{A3})$$

The function can be defined based on the homogenous Airy functions:

$$\text{Gi}(x) = \text{Bi}(x) \int_x^\infty \text{Ai}(t) dt + \text{Ai}(x) \int_0^x \text{Bi}(t) dt \quad (\text{A4})$$

The general solution can be written as:

$$y(x) = a\text{Ai}(x) + b\text{Bi}(x) + \text{Gi}(x) \quad (\text{A5})$$

The shape equation (eqn (19)) in terms of curvature can be compared with the second Painleve equation, $y'' = zy + by^3 + a$:

$$\kappa'' = \underbrace{\left[\frac{\gamma_0}{k_c} - \frac{W}{2k_c}(\cos^2(\varphi - \theta)) - \frac{W}{k_c}(\sin^2(\varphi - \theta)) \right]}_{f(s)\kappa} \kappa - \frac{1}{2}\kappa^3 + \underbrace{\frac{-\Delta p}{k_c}}_a \quad (\text{A6})$$

The second Painleve equation can be considered as a non-linear generalization of the Airy equation. For the case $a = 1/2$, the solution to the equation can be expressed with the Airy function. The function $K(x, y)$ is introduced as the solution to homogenous Painleve equation, $y'' = zy + 2\sigma y^3$:⁵⁵

$$K(x, y) = r\text{Ai}\left(\frac{x+y}{2}\right) + \sigma \frac{r^2}{4} \int_x^\infty \int_x^\infty K(x, z) \text{Ai}\left(\frac{z+s}{2}\right) \text{Ai}\left(\frac{s+y}{2}\right) dz ds \quad (\text{A7})$$

where $y \geq x$, $\sigma = \pm 1$, and r is a parameter. Under the condition that $z \rightarrow \infty$, W behaves like the Airy function:

$$y(z; r) \approx r\text{Ai}(z) \quad (\text{A8})$$

Under the condition that $k_c \rightarrow 0$, the shape equation (eqn (A6)) behaves like an inhomogeneous Airy function, $y'' = zy + a$.

Fig. 12 and 13 clearly show the comparison between the dimensionless curvature of the liquid crystal membranes and the Airy transformations that can be defined as a family of functions:

$$\omega_\alpha(s) = \frac{c_1}{\alpha} \text{Ai}\left(\frac{s}{\alpha} + \frac{c_2}{\alpha}\right), \quad \alpha \in \mathbb{R} \quad (\text{A9})$$

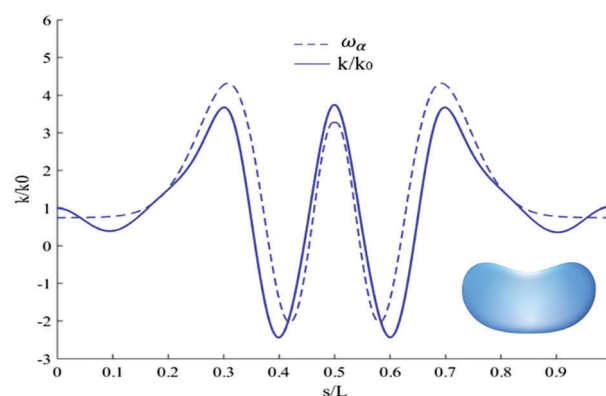


Fig. 12 Comparison between scaled curvature of a liquid crystal membrane (stomatocyte morphology) and the Airy function.

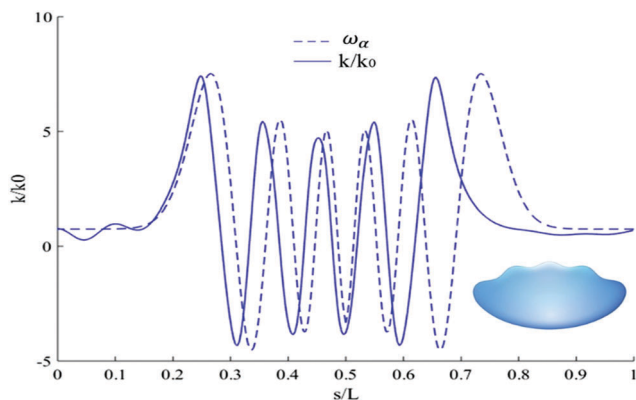


Fig. 13 The comparison between scaled curvature of a liquid crystal membrane (undulate morphology) and Airy function.

c_1 and c_2 are coefficient to be determined. We can readily realize that Airy functions are a good approximation for the membrane curvature.

Acknowledgements

Financial support for this research was provided by the Natural Science and Engineering Research Council of Canada (NSERC) and Le Fonds Quebecois de la Recherche sur la Nature et les Technologies (FRQNT). PR is grateful for a MEDA scholarship from McGill's Faculty of Engineering. ADR is grateful for financial support through the James McGill Professorship appointment.

References

- (a) J. B. Bostwick, M. J. Miksis and S. H. Davis, Elastic membranes in confinement, *J. R. Soc., Interface*, 2016, **13**(120), 201604; (b) U. Seifert, Configurations of fluid membranes and vesicles, *Adv. Phys.*, 1997, **46**(1), 13–137; (c) S. K. Veerapaneni, R. Raj, G. Birocs and P. K. Purohit, Analytical and numerical solutions for shapes of quiescent two-dimensional vesicles, *Int. J. NonLinear Mech.*, 2009, **44**(3), 257–262; (d) L. Giomi, Softly constrained films, *Soft Matter*, 2013, **9**(34), 8121–8139; (e) V. M. Vassilev, P. A. Djondjorov and I. M. Mladenov, Cylindrical equilibrium shapes of fluid membranes, *J. Phys. A: Math. Theor.*, 2008, **41**(43), 435201.
- K. Khairy, J. Foo and J. Howard, Shapes of Red Blood Cells: Comparison of 3D Confocal Images with the Bilayer-Couple Model, *Cell. Mol. Bioeng.*, 2008, **1**(2–3), 173–181.
- (a) V. Heinrich, S. Svetina and B. Zeks, Nonaxisymmetric Vesicle Shapes in a Generalized Bilayer-Couple Model and the Transition between Oblate and Prolate Axisymmetrical Shapes, *Phys. Rev. E: Stat. Phys., Plasmas, Fluids, Relat. Interdiscip. Top.*, 1993, **48**(4), 3112–3123; (b) H. W. G. Lim, M. Wortis and R. Mukhopadhyay, Stomatocyte-discocyte-echinocyte sequence of the human red blood cell: Evidence for the bilayer-couple hypothesis from membrane mechanics, *Proc. Natl. Acad. Sci. U. S. A.*, 2002, **99**(26), 16766–16769.
- (a) A. J. Markvoort, R. A. van Santen and P. A. J. Hilbers, Vesicle shapes from molecular dynamics simulations, *J. Phys. Chem. B*, 2006, **110**(45), 22780–22785; (b) J. Y. Su, Z. W. Yao and M. O. de la Cruz, Vesicle Geometries Enabled by Dynamically Trapped States, *ACS Nano*, 2016, **10**(2), 2287–2294.
- K. Khairy and J. Howard, Minimum-energy vesicle and cell shapes calculated using spherical harmonics parameterization, *Soft Matter*, 2011, **7**(5), 2138–2143.
- X. J. Li, Shape transformations of bilayer vesicles from amphiphilic block copolymers: a dissipative particle dynamics simulation study, *Soft Matter*, 2013, **9**(48), 11663–11670.
- (a) L. S. Hirst, A. Ossowski, M. Fraser, J. Geng, J. V. Selinger and R. L. B. Selinger, Morphology transition in lipid vesicles due to in-plane order and topological defects, *Proc. Natl. Acad. Sci. U. S. A.*, 2013, **110**(9), 3242–3247; (b) T. Gibaud, E. Barry, M. J. Zakhary, M. Henglin, A. Ward, Y. S. Yang, C. Berciu, R. Oldenbourg, M. F. Hagan, D. Nicastro, R. B. Meyer and Z. Dogic, Reconfigurable self-assembly through chiral control of interfacial tension, *Nature*, 2012, **481**(7381), 348–351; (c) E. H. Yong, D. R. Nelson and L. Mahadevan, Elastic Platonic Shells, *Phys. Rev. Lett.*, 2013, **111**(17), 177801; (d) G. Vernizzi, R. Sknepnek and M. O. de la Cruz, Platonic and Archimedean geometries in multicomponent elastic membranes, *Proc. Natl. Acad. Sci. U. S. A.*, 2011, **108**(11), 4292–4296.
- L. Tayebi, Y. C. Ma, D. Vashae, G. Chen, S. K. Sinha and A. N. Parikh, Long-range interlayer alignment of intralayer domains in stacked lipid bilayers, *Nat. Mater.*, 2012, **11**(12), 1074–1080.
- F. Livolant and A. Leforestier, Condensed phases of DNA: Structures and phase transitions, *Prog. Polym. Sci.*, 1996, **21**(6), 1115–1164.
- E. Belamie, G. Mosser, F. Gobeaux and M. M. Giraud-Guille, Possible transient liquid crystal phase during the laying out of connective tissues: alpha-chitin and collagen as models, *J. Phys.: Condens. Matter*, 2006, **18**(13), 115–129.
- A. C. Neville, *Biology of fibrous composites: development beyond the cell membrane*, Cambridge University Press, New York, NY, USA, 1993, p. 214, vii.
- M. M. Giraudguille, Twisted Plywood Architecture of Collagen Fibrils in Human Compact-Bone Osteons, *Calcif. Tissue Int.*, 1988, **42**(3), 167–180.
- (a) S. Jordens, L. Isa, I. Usov and R. Mezzenga, Non-equilibrium nature of two-dimensional isotropic and nematic coexistence in amyloid fibrils at liquid interfaces, *Nat. Commun.*, 2013, **4**, 1917; (b) S. Jordens, K. Schwenke, I. Usov, E. Del Gado and R. Mezzenga, Nematic field transfer in a two-dimensional protein fibril assembly, *Soft Matter*, 2016, **12**(6), 1830–1835.
- Y. Bouligand, Liquid crystals and biological morphogenesis: Ancient and new questions, *C. R. Chim.*, 2008, **11**(3), 281–296.
- R. C. Sarasij, S. Mayor and M. Rao, Chirality-induced budding: A raft-mediated mechanism for endocytosis and morphology of caveolae?, *Biophys. J.*, 2007, **92**(9), 3140–3158.

- 16 H. T. McMahon and J. L. Gallop, Membrane curvature and mechanisms of dynamic cell membrane remodelling, *Nature*, 2005, **438**(7068), 590–596.
- 17 D. Bruggemann, J. P. Frohnmayer and J. P. Spatz, Model systems for studying cell adhesion and biomimetic actin networks, *Beilstein J. Nanotechnol.*, 2014, **5**, 1193–1202.
- 18 T. S. Nguyen, J. Geng, R. L. B. Selinger and J. V. Selinger, Nematic order on a deformable vesicle: theory and simulation, *Soft Matter*, 2013, **9**(34), 8314–8326.
- 19 J. M. Brake, M. K. Daschner, Y. Y. Luk and N. L. Abbott, Biomolecular interactions at phospholipid-decorated surfaces of liquid crystals, *Science*, 2003, **302**(5653), 2094–2097.
- 20 L. N. Tan and N. L. Abbott, Dynamic anchoring transitions at aqueous-liquid crystal interfaces induced by specific and non-specific binding of vesicles to proteins, *J. Colloid Interface Sci.*, 2015, **449**, 452–461.
- 21 (a) R. Zhang, Y. Zhou, J. A. Martinez-Gonzalez, J. P. Hernandez-Ortiz, N. L. Abbott and J. J. de Pablo, Controlled deformation of vesicles by flexible structured media, *Sci. Adv.*, 2016, **2**(8), e1600978; (b) L. S. Hirst, J. Geng, A. Ossowski, M. Fraser, J. V. Selinger and R. L. B. Selinger, Morphology Transition in Lipid Vesicles: Interaction of In-Plane Order and Topological Defects, *Biophys. J.*, 2013, **104**(2), 3242–3247.
- 22 S. A. Safran, *Statistical thermodynamics of surfaces, interfaces, and membranes*, Addison-Wesley Pub., Reading, Mass., 1994, p. 270, xvii.
- 23 (a) L. K. E. A. Abdelmohsen, D. S. Williams, J. Pille, S. G. Ozel, R. S. M. Rikken, D. A. Wilson and J. C. M. van Hest, Formation of Well-Defined, Functional Nanotubes via Osmotically Induced Shape Transformation of Biodegradable Polymersomes, *J. Am. Chem. Soc.*, 2016, **138**(30), 9353–9356; (b) K. A. Simon, P. Sejwal, R. B. Gerecht and Y. Y. Luk, Water-in-water emulsions stabilized by non-amphiphilic interactions: Polymer-dispersed lyotropic liquid crystals, *Langmuir*, 2007, **23**(3), 1453–1458.
- 24 (a) F. C. Mackintosh and T. C. Lubensky, Orientational Order, Topology, and Vesicle Shapes, *Phys. Rev. Lett.*, 1991, **67**(9), 1169–1172; (b) S. V. Lishchuk and C. M. Care, Shape of an isotropic droplet in a nematic liquid crystal: The role of surfactant, *Phys. Rev. E: Stat., Nonlinear, Soft Matter Phys.*, 2004, **70**(1), 011702; (c) P. Prinsen and P. van der Schoot, Shape and director-field transformation of tactoids, *Phys. Rev. E: Stat., Nonlinear, Soft Matter Phys.*, 2003, **68**(2), 021701.
- 25 J. Jeong, Z. S. Davidson, P. J. Collings, T. C. Lubensky and A. G. Yodh, Chiral symmetry breaking and surface faceting in chromonic liquid crystal droplets with giant elastic anisotropy, *Proc. Natl. Acad. Sci. U. S. A.*, 2014, **111**(5), 1742–1747.
- 26 F. C. Keber, E. Loiseau, T. Sanchez, S. J. DeCamp, L. Giomi, M. J. Bowick, M. C. Marchetti, Z. Dogic and A. R. Bausch, Topology and dynamics of active nematic vesicles, *Science*, 2014, **345**(6201), 1135–1139.
- 27 A. A. Verhoeff, I. A. Bakelaar, R. H. J. Otten, P. van der Schoot and H. N. W. Lekkerkerker, Tactoids of Plate-Like Particles: Size, Shape, and Director Field, *Langmuir*, 2011, **27**(1), 116–125.
- 28 J. Rudnick and R. Bruinsma, Shape of Domains in 2-Dimensional Systems – Virtual Singularities and a Generalized Wulff Construction, *Phys. Rev. Lett.*, 1995, **74**(13), 2491–2494.
- 29 Y. K. Kim, S. V. Shiyankovskii and O. D. Lavrentovich, Morphogenesis of defects and tactoids during isotropic-nematic phase transition in self-assembled lyotropic chromonic liquid crystals, *J. Phys.: Condens. Matter*, 2013, **25**(40), 404202.
- 30 K. S. Krishnamurthy, P. Kumar, N. B. Palakurthy, C. V. Yelamaggad and E. G. Virga, Interfacial and morphological features of a twist-bend nematic drop, *Soft Matter*, 2016, **12**(22), 4967–4978.
- 31 (a) A. G. Cheong and A. D. Rey, Temperature effects on capillary instabilities in a thin nematic liquid crystalline fiber embedded in a viscous matrix, *Eur. Phys. J. E: Soft Matter Biol. Phys.*, 2002, **9**(2), 171–193; (b) A. G. Cheong and A. D. Rey, Capillary instabilities in a thin nematic liquid crystalline fiber embedded in a viscous matrix, *Continuum Mech. Thermodyn.*, 2002, **14**(3), 263–279; (c) A. G. Cheong and A. D. Rey, Cahn-Hoffman capillarity vector thermodynamics for curved liquid crystal interfaces with applications to fiber instabilities, *J. Chem. Phys.*, 2002, **117**(10), 5062–5071; (d) A. G. Cheong and A. D. Rey, Cahn-Hoffman capillarity vector thermodynamics for liquid crystal interfaces, *Phys. Rev. E: Stat., Nonlinear, Soft Matter Phys.*, 2002, **66**(2), 021704; (e) A. G. Cheong and A. D. Rey, Texture dependence of capillary instabilities in nematic liquid crystalline fibres, *Liq. Cryst.*, 2004, **31**(9), 1271–1284; (f) P. Rofouie, D. Pasini and A. D. Rey, Nanostructured free surfaces in plant-based plywoods driven by chiral capillarity, *Colloid Interface Sci. Commun.*, 2014, **1**, 23–26; (g) P. Rofouie, D. Pasini and A. D. Rey, Tunable nano-wrinkling of chiral surfaces: Structure and diffraction optics, *J. Chem. Phys.*, 2015, **143**(11), 114701; (h) P. Rofouie, D. Pasini and A. D. Rey, Nano-scale surface wrinkling in chiral liquid crystals and plant-based plywoods, *Soft Matter*, 2015, **11**(6), 1127–1139; (i) P. Rofouie, D. Pasini and A. D. Rey, Multiple-wavelength surface patterns in models of biological chiral liquid crystal membranes, *Soft Matter*, 2017, **13**, 514–545; (j) A. D. Rey, Mechanics of soft-solid-liquid-crystal interfaces, *Phys. Rev. E: Stat., Nonlinear, Soft Matter Phys.*, 2005, **72**(1), 011706.
- 32 A. Rapini and M. Papoular, Distorsion d'une lamelle nématique sous champ magnétique conditions d'ancrage aux parois, *J. Phys., Colloq.*, 1969, **30**, 54–56.
- 33 W. Helfrich, Elastic Properties of Lipid Bilayers – Theory and Possible Experiments, *Z. Naturforsch., C: J. Biosci.*, 1973, **C28**(11), 693–703.
- 34 (a) H. Jinnai, Y. Nishikawa and T. Hashimoto, Curvature distributions of spinodal interface in a condensed matter system, *Phys. Rev. E: Stat. Phys., Plasmas, Fluids, Relat. Interdiscip. Top.*, 1999, **59**(3), R2554–R2557; (b) D. Kammer and P. W. Voorhees, The morphological evolution of

- dendritic microstructures during coarsening, *Acta Mater.*, 2006, **54**(6), 1549–1558.
- 35 S. N. Krivoschapko and V. N. Ivanov, SpringerLink (Online service), Encyclopedia of Analytical Surfaces, p. 29, 752.
 - 36 F. Chang and K. C. Huang, How and why cells grow as rods, *BMC Biol.*, 2014, **12**, 54.
 - 37 D. W. Hoffman and J. W. Cahn, Vector Thermodynamics for Anisotropic Surfaces 1. Fundamentals and Application to Plane Surface Junctions, *Surf. Sci.*, 1972, **31**(1), 368–388.
 - 38 Y. Q. Bai and N. L. Abbott, Recent Advances in Colloidal and Interfacial Phenomena Involving Liquid Crystals, *Langmuir*, 2011, **27**(10), 5719–5738.
 - 39 A. D. Rey, Thermodynamic model of surfactant adsorption on soft liquid crystal interfaces, *Langmuir*, 2004, **20**(26), 11473–11479.
 - 40 (a) A. D. Rey, Capillary models for liquid crystal fibers, membranes, films, and drops, *Soft Matter*, 2007, **3**(11), 1349–1368; (b) A. D. Rey, Line tension vector thermodynamics of anisotropic contact lines, *Phys. Rev. E: Stat., Nonlinear, Soft Matter Phys.*, 2004, **69**(4), 041707.
 - 41 P.-G. D. Gennes and J. Prost, *The physics of liquid crystals*, Clarendon Press, Oxford University Press, Oxford New York, 2nd edn, 1995, p. 597, xvi.
 - 42 R. Meister, H. Dumoulin, M. A. Halle and P. Pieranski, Anchoring of a cholesteric liquid crystal at the free surface, *J. Phys. II*, 1996, **6**(6), 827–844.
 - 43 D. H. Boal, *Mechanics of the cell*, Cambridge University Press, Cambridge, New York, 2nd edn, 2012, p. 608, xiv.
 - 44 M. Ghochani, J. D. Nulton, P. Salamon, T. G. Frey, A. Rabinovitch and A. R. C. Baljon, Tensile Forces and Shape Entropy Explain Observed Crista Structure in Mitochondria, *Biophys. J.*, 2010, **99**(10), 3244–3254.
 - 45 C. J. Vogl, M. J. Miksis, S. H. Davis and D. Salac, The effect of glass-forming sugars on vesicle morphology and water distribution during drying, *J. R. Soc., Interface*, 2014, **11**(99), 20140646.
 - 46 H. S. M. Coxeter, *Introduction to geometry*, Wiley, New York, 2nd edn, 1969, p. 469, xvi.
 - 47 (a) R. Eelkema, M. M. Pollard, N. Katsonis, J. Vicario, D. J. Broer and B. L. Feringa, Rotational reorganization of doped cholesteric liquid crystalline films, *J. Am. Chem. Soc.*, 2006, **128**(44), 14397–14407; (b) A. D. Rey, Viscoelastic theory for nematic interfaces, *Phys. Rev. E: Stat. Phys., Plasmas, Fluids, Relat. Interdiscip. Top.*, 2000, **61**(2), 1540–1549.
 - 48 A. D. Rey, Thermodynamics of soft anisotropic interfaces, *J. Chem. Phys.*, 2004, **120**(4), 2010–2019.
 - 49 A. D. Rey, Mechanical model for anisotropic curved interfaces with applications to surfactant-laden liquid–liquid crystal interfaces, *Langmuir*, 2006, **22**(1), 219–228.
 - 50 E. Doedel and B. Oldeman, Auto-07p: Continuation and Bifurcation Software for Ordinary Differential Equations, 2012.
 - 51 H. Aharoni, Y. Abraham, R. Elbaum, E. Sharon and R. Kupferman, Emergence of Spontaneous Twist and Curvature in Non-Euclidean Rods: Application to Erodium Plant Cells, *Phys. Rev. Lett.*, 2012, **108**(23), 238106.
 - 52 A. D. Rey and M. M. Denn, Jeffrey-Hamel Flow of Leslie-Ericksen Nematic Liquids, *J. Non-Newtonian Fluid Mech.*, 1988, **27**(3), 375–401.
 - 53 R. M. W. van Bijnen, R. H. J. Otten and P. van der Schoot, Texture and shape of two-dimensional domains of nematic liquid crystals, *Phys. Rev. E: Stat., Nonlinear, Soft Matter Phys.*, 2012, **86**(5), 051703.
 - 54 E. G. Virga, *Variational theories for liquid crystals*, Chapman & Hall, London, New York, 1st edn, 1994, p. 375, xii.
 - 55 O. Vallée and M. Soares, *Airy functions and applications to physics*, Imperial College Press, London Hackensack distributed by World Scientific, 2nd edn, 2010, p. 202, x.